electronic reprint

Journal of
Synchrotron Radiation
ISSN 0909-0495
Editors: **Å. Kvick, D. M. Mills and T. Ohta**

An X-ray nanodiffraction technique for structural characterization of individual nanomaterials

Y. Xiao, Z. Cai, Z. L. Wang, B. Lai and Y. S. Chu

Copyright © International Union of Crystallography

Author(s) of this paper may load this reprint on their own web site provided that this cover page is retained. Republication of this article or its storage in electronic databases or the like is not permitted without prior permission in writing from the IUCr.

Journal of
Synchrotron
Radiation

ISSN 0909-0495

Received 8 June 2004
Accepted 5 November 2004

An X-ray nanodiffraction technique for structural characterization of individual nanomaterials

Y. Xiao,[a] Z. Cai,[a]* Z. L. Wang,[b] B. Lai[a] and Y. S. Chu[a]

[a]Experimental Facilities Division, Argonne National Laboratory, Argonne, IL 60439, USA, and [b]School of Materials Science and Engineering, Georgia Institute of Technology, Atlanta, GA 30332-0245, USA. E-mail: cai@aps.anl.gov

An X-ray micro/nanodiffraction technique that allows structural characterization of individual nanomaterials has been developed at an insertion-device beamline of the Advanced Photon Source. Using the extremely high brightness of the third-generation synchrotron radiation source and advanced high-resolution high-energy zone-plate focusing optics, X-rays of energies from 6 to 12 keV have been focused into a spot smaller than 200 nm with a photon density gain of more than 50000 so that significant photon flux can be intercepted by a nanoscale material to generate a measurable diffraction signal for structural characterization. This paper describes the instrumentation of the technique and discusses the application of the technique to studies of tin oxide nanobelts.

© 2005 International Union of Crystallography
Printed in Great Britain – all rights reserved

Keywords: X-ray microprobe; X-ray nanodiffraction.

1. Introduction

Although the potential of an X-ray microprobe was recognized more than 30 years ago and many applications of the technique have been pursued since then, limited focal flux of the beam and spatial resolution due to low source brightness and poor performance of X-ray optics had prevented this technique from being widely used. Until the availability of third-generation synchrotron radiation not long ago and development of X-ray microfocusing optics largely encouraged by the new source, X-ray microprobe techniques, such as X-ray microdiffraction, microfluorescence and microspectroscopy, begin to become mature and are now being applied in materials sciences (Soh *et al.*, 2002; Eastman *et al.*, 2002), solid-state physics (Evans *et al.*, 2002), bio and medical sciences (Dillon *et al.*, 2002; Hall *et al.*, 2003), environmental sciences (Yun *et al.*, 1998) and many other disciplines. However, X-ray scattering characterizations of nanoscale materials have been performed so far on the basis of summing information obtained by illuminating a large number of nanomaterials (Wang *et al.*, 2002, 2003; Chen *et al.*, 2003; Wen *et al.*, 2002; Maniwa *et al.*, 2003; Goldberger *et al.*, 2003; Liu, Yue & Wehmschulte, 2002; Liu, Dong & Wang, 2002; Xu *et al.*, 2003; Arabatzis & Falaras, 2003; Raola & Strouse, 2002) because not enough photons in an X-ray microbeam would be intercepted by a single nano-object to generate measurable signals. This technique would be useful only if high uniformity of structures among the nanomaterials exist. Detailed local information, such as nanostructure or structure variation within individual nanomaterials and dimension-dependent structural properties, would be lost after averaging the information from an assembly of a large amount of objects with various sizes. Therefore, a tool capable of structural characterization of individual nanomaterials with high sensitivity, high penetrative power and nondestruction is in high demand.

When the dimensions of particles become smaller than the focal spot sizes of currently available X-ray optics, the photon flux density reflects the capacity for a nanosample to intercept photons. Fresnel zone plates (Yun *et al.*, 1992; Lai *et al.*, 1992), Kirkpatrick–Baez mirrors (Kirkpatrick & Baez, 1948; Howells, 1995) and refractive compound lenses (Snigirev *et al.*, 1996) are commonly employed X-ray focusing optics; all are capable of micrometer or submicrometer focusing. Owing to the perfectness of its optical features resulting from the highly mature stage of manufacturing, a zone plate is the most promising optics to provide X-ray beams of the highest photon flux density. Taking full advantage of the brightest synchrotron radiation source and state-of-the-art zone-plate X-ray focusing optics, we developed, at the Advanced Photon Source (APS), an X-ray nanodiffraction technique that allows studies of the material structure of a single nanoscale object.

Recently, a new group of semiconducting oxide (tin oxide, zinc oxide, indium oxide and cadmium oxide) nanostructures that have a belt-like morphology (rectangular cross section) have been synthesized *via* a thermal evaporation and condensation process (Pan *et al.*, 2001). The synthesis is based on thermal evaporation of oxide powders under controlled conditions without the presence of a catalyst. The belt-like geometrical morphology is a common structural characteristic for these oxides with different crystallographic structures. We select tin oxide nanobelts for the demonstration of the X-ray nanodiffraction technique because the system has well defined characteristics including its crystallographic structure and dimensions. In this paper we describe the application of the

electronic reprint

nanodiffraction technique to the structural determination of tin oxide nanobelt crystals.

2. Experimental

X-ray nanodiffraction was developed at the 2-ID-D station of the APS. A hard X-ray microprobe (HXRM) focuses the radiation generated from APS undulator A (Dejus *et al.*, 2002) to a spot size limited by the outmost zone width of the zone-plate optics. Fig. 1 schematically illustrates the configuration of the microprobe. In order to preserve the brilliance of the X-ray source and the beam coherence, and to suppress high-order harmonics of the undulator radiation, a water-cooled grazing-incidence horizontal-deflection mirror is used to take the high heat load of the radiation power. A double-crystal Si(111) monochromator is used to select the energy of X-rays from 5.5 keV to 30 keV with a relative bandwidth of 10^{-4}. The HXRM employs a gold zone plate of size 150 μm and focal length 10 cm (at 8 keV) and is placed at a distance 74 m from the source. The zone plate has an outmost zone width of 0.1 μm and a focal efficiency of 13%. Photon flux of more than 10^9 photons s^{-1} (0.01% bandwidth)$^{-1}$ can be achieved at the focal spots of 150 nm × 150 nm, which corresponds to a photon density gain of 10^5 (Cai *et al.*, 2000). A two-zone-plate stacking technique could be employed in the HXRM to further improve focusing efficiency and extend the zone-plate micro-focusing capability into higher energy. To suppress radiation background as much as possible for a better detection limit, a circular order-sorting aperture of 20 μm and a gold beam stopper (30 μm in diameter and 40 μm thick) are used to select the first-order focusing beam and reduce the zero-order beam through the 20 μm order-sorting aperture. The selection of the horizontal coherence length and thus the horizontal focal spot size is realised by use of a white-beam slit located 28 m from the source.

The HXRM was further integrated with a six-circle kappa geometry diffractometer (Libera *et al.*, 2002; Cai *et al.*, 2003), as shown in Fig. 2. The closed-loop servodrivers with on-axis encoders provide angular resolution of 0.0001° for sample and detector circles and 0.00025° for circles that carry the sample-circle assembly and detector-arm assembly. Experimental results indicated that the repeatability of the angular motion of the circles is better than 0.001°. With careful design of the HXRM's supporting structure and vibration-damping mechanism for isolation of vibration from the experimental floor, we have demonstrated a focal spot size better than 190 nm.

Detectors used in the nanodiffraction systems are a CCD area detector with a field of view of 60 mm × 60 mm and effective pixel size of 50 μm, a NaI counting detector and a silicon energy-dispersive detector for X-ray fluorescence measurements. The silicon detector is used to locate a nano-object in the sample and monitor the relative stability between the positions of the focal spot and the nano-object.

The tin oxide nanobelts used for the studies were synthesized using thermal evaporation of either SnO_2 powders (purity: 99.9%; melting point: 1903 K) at 1623 K or SnO powders (purity: 99.9%; melting point: 1353 K) at 1273 K under controlled conditions without the presence of a catalyst. These conditions include a chamber pressure of 300 torr, an Ar flowing rate of 50 standard cubic centimeters per minute and an evaporation time of 120 min (Pan *et al.*, 2001). Synthesized nanobelts have a rectangle-like cross section with

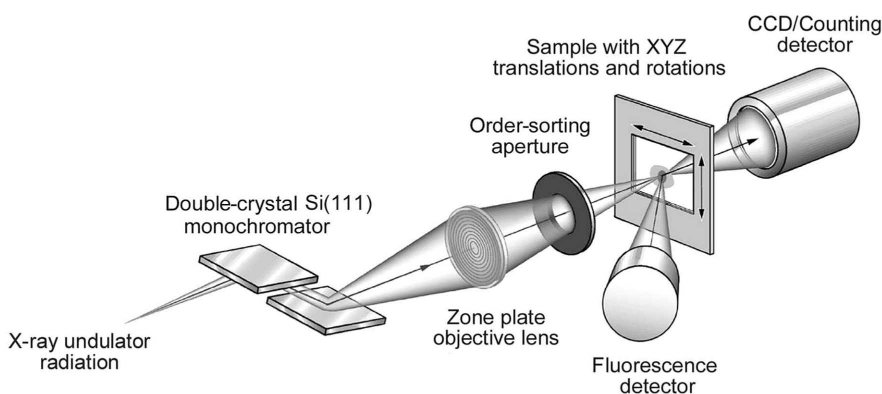

Figure 1
Schematic of the X-ray microprobe at the 2-ID-D station of the APS.

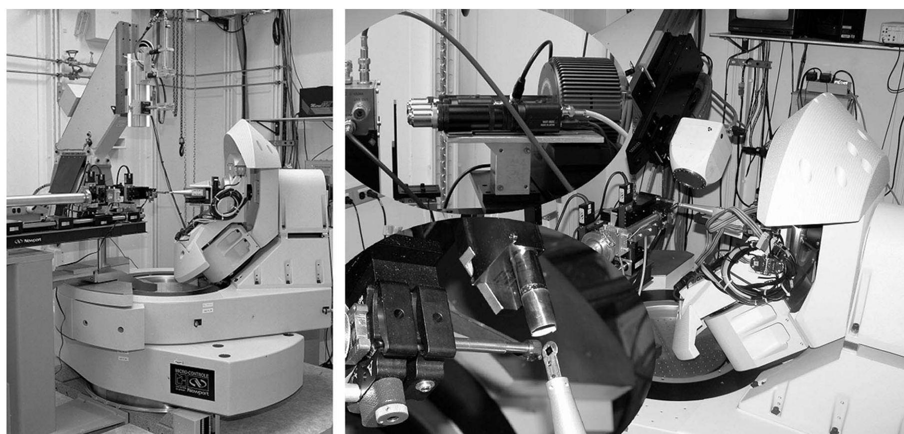

Figure 2
Integration of the X-ray microprobe with the six-circle diffractometer (left) and the nanodiffraction experiment setup (right). The lower left inset of the right-hand image displays the microbe assembly containing beam stop, zone plate and order-sorting aperture along with sample holder and fluorescence detector. The upper left inset of the right-hand image is the assembly of the X-ray scintillator imaging system located downstream of the diffractometer for microprobe and sample alignment.

electronic reprint

a typical width of 30–300 nm, width-to-thickness ratios of 3–10 and lengths of up to a few millimeters.

Given the size of the tin oxide nanobelts, it is difficult to position the sample in the microbeam since there is no X-ray absorption contrast from the material at the working energy. In order to select individual nanobelts from the as-synthesized material, we first dispersed the nanobelts in an ethyl-alcohol solution and transfer them onto a flat silicon nitride window (2 mm × 2 mm size and 500 nm thickness) coated with a gold mesh of 200 µm per grid. The concentration of the nanobelts is diluted so that the nanobelts are well separated from each other on the silicon nitride film. The coated gold mesh on the silicon nitride window has enough absorption contrast to serve as an internal reference so that the X-ray microbeam can be delivered to a selected nanobelt. Then, a scanning electron microscope (SEM) was used to characterize the widths and lengths of nanobelts and establish coordinates of selected belts against the gold mesh. A 10–20 nm-thick layer of carbon was deposited on the samples for electric conductivity to reduce the charging effect in the SEM.

3. Results

Photon flux density is an important parameter directly affecting the possibility of nanodiffraction. Total focal flux is determined by the size of the zone plate and the focal efficiency of the zone plate, which depends on the energy of the X-rays. After the zone plate and the X-ray energy are selected, the focal spot size is a direct measure of the photon flux density. The measurement of the focal spot size was performed by measuring the Sn *L*-line fluorescence profiles obtained from a 100 nm tin oxide nanobelt held on the sample assembly of the diffractometer while it was scanned across the X-ray beam at the focal plane. In Fig. 3 we show the measured horizontal zinc fluorescence profiles, which indicate a spot size smaller than 200 nm FWHM. Since the measured beam spot size is a convolution of the true spot size with the width of the nanobelt, step width of the scanning stage, and the mechanical instability of the microprobe–diffractometer integration, the value indicated in the figure only serves as an upper limit of the true beam spot size.

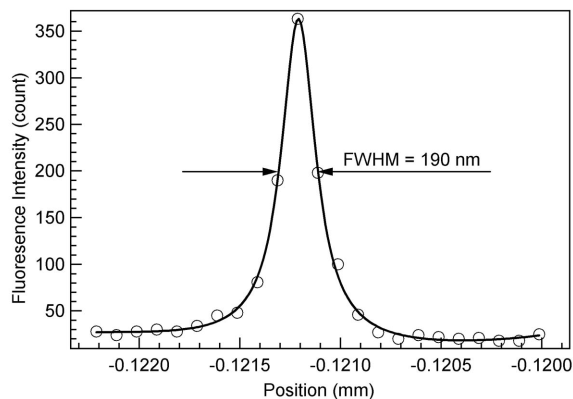

Figure 3
Sn *L*-line fluorescence profile (open circles) obtained from exciting a 100 nm tin oxide nanobelt with 7.0 keV X-rays while the nanobelt is horizontally scanned across the focused beam. The solid line is the fit to the measured data with the Vogt function, indicating an upper-limit beam spot of less than 200 nm.

The crystallographic structure of the tin oxide nanobelts was determined to be triclinic (Sn_2O_3) by X-ray diffraction from individual nanocrystals. The unit-cell parameters of the triclinic tin oxide are $a = 5.457$, $b = 8.179$, $c = 3.714$ Å, $\alpha = 93.8$, $\beta = 92.3$ and $\gamma = 90°$ (Murken & Tromel, 1973). Bragg reflections from atomic planes (030), (011) and ($0\bar{2}1$) were measured by rotating the crystal around an axis along the width. Not only did the 2θ angles of the reflections match the value of the 2θ angles calculated from the unit-cell parameters at the energy of the measurement, but also the differences of θ angles between any two of the three reflections matched those calculated. From the orientations of the nanobelts at which the three reflections appeared, we further determined that the triclinic tin oxide nanobelts grow along [001] and are enclosed by ±(010) and ±(100) crystallographic facets.

Samples of the nanobelts were prepared so that separation of the nanobelts is much larger than the beam spot size, and no more than one belt would be illuminated at the same time. In Fig. 4 we display resolution-limited maps of the tin fluorescence intensity and the diffraction intensity of the (030) reflection against the sample position in the transverse plane on which the nanobelts lie. The map of the diffraction intensity matches the map of the fluorescence intensity, confirming that the diffraction is from a single nanobelt.

The distribution of the diffraction intensity in reciprocal space contains information on the nanostructure within a nanomaterial. In order to further study subgrain structure in Sn_2O_3 nanobelts, we used a CCD area detector to capture the (030) reflection from Sn_2O_3 nanobelts. In Fig. 5 we show diffraction patterns of the reflection obtained from a 100 nm

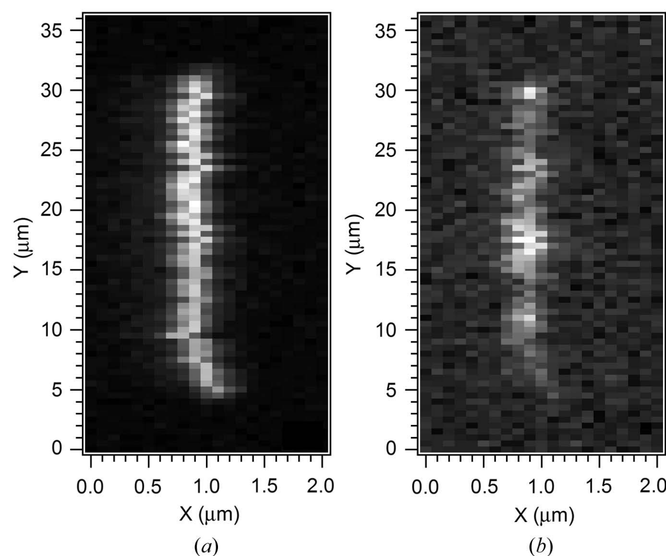

Figure 4
Two-dimensional mapping of the tin *L*-lines fluorescence intensity (*a*) and the diffraction intensity of the (030) reflection (*b*) from a 100 nm-width tin oxide nanobelt. The maximum intensity per pixel in (*a*) is 450 counts and that in (*b*) is 60000 counts.

electronic reprint

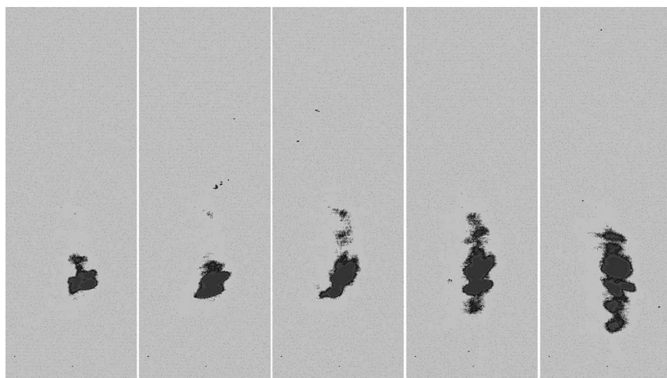

Figure 5
X-ray diffraction spots of the (030) reflection from a 100 nm Sn_2O_3 nanobelt captured by a CCD detector. Starting from the left, each image was taken after a translation of the microbeam along the length of the nanobelt in steps of 200 nm. The first image is the diffraction spot obtained when the end of the belt was illuminated. The horizontal axis represents the 2θ direction and ranges from 36.5 to 39.5°. The vertical axis represents the χ direction and covers 8.5°.

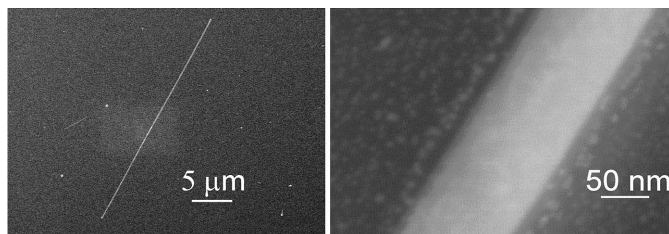

Figure 6
SEM images of a tin oxide nanobelt of size 30 μm × 100 nm with secondary electrons (left) and backscattering electrons (right).

tin oxide nanobelt. The diffraction patterns are clearly composed of several subspots splitting along the χ direction over a range of degrees, indicating a subgrain with highly textured structure in the nanobelt. The splitting of the diffraction spots along the θ direction is much smaller that the splitting along the χ direction, suggesting a relatively small strain variation among grains. Further studies of the grain orientation distribution along the θ direction revealed a three to five times smaller distribution of grain orientation around the θ axis than around the χ axis.

When the dimensions of a nanomaterial fall into a region in which the material properties depend on the dimensions, the characterization of the dimensions of a nanomaterial becomes important in materials studies. The high penetration power of X-rays into the materials is an advantage for embedded nanomaterials. Although SEM is an accurate tool for size characterization of unembedded materials in the plane normal to the electron beam, accurate measurement of the extent of the material along the third dimension sometimes requires better techniques like X-ray scattering. In order to measure the thickness of a 100 nm tin oxide nanobelt, we performed an X-ray radial scan across the (030) point in the reciprocal space. In Figs. 6 and 7 we display the SEM images of a tin oxide nanobelt of size 30 μm × 100 nm and the X-ray θ–2θ profiles along the (030) reflection of the same tin oxide belt. Using

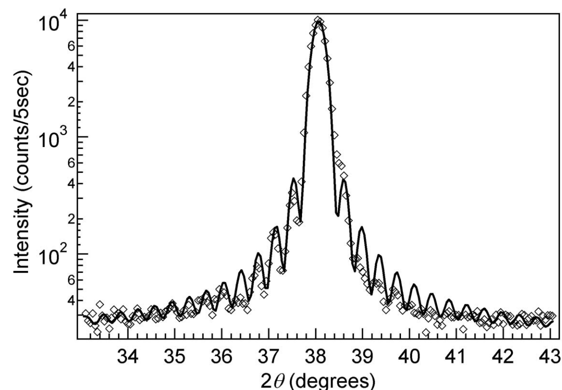

Figure 7
Measured (open diamonds) and calculated (solid line) X-ray θ–2θ scan profiles of the (030) reflection from the 100 nm triclinic tin oxide nanobelt shown in Fig. 6. The calculation is based on the kinematic scattering theory, the lateral dimensions determined with SEM, and the single-lattice arrangement of atomic positions with a parameter of the number of atomic layers. The interference fringes and their frequency characterize the thickness of the nanobelt. The fitting of the profile led to a thickness of 29 nm.

7.0 keV X-rays and with a 2θ angular resolution of 8.6×10^{-4} rad we found that the incident angle θ for the (030) reflection measured from the surface of the silicon nitride membrane is almost identical to the theoretical value for the Bragg reflection, indicating that the surfaces of the nanobelt shown in the SEM micrographs are truncated with the (010) atomic plane. With the widths determined by SEM, a theoretically calculated reflectivity profile (solid line in Fig. 7) based on the kinematic scattering theory and single-lattice arrangement of atomic positions with a parameter of number of atomic layers was used to fit the measured profiles to obtain the thickness of the nanobelt. The fitting of the profile led to a thickness of 29 nm.

In conclusion, we have developed and demonstrated an X-ray nanodiffraction technique at the Advanced Photon Source that allows the study of structures of nanomaterials on a single object. The technique has enabled us to study nanostructure and its dependence on material dimensions in a single nanobelt of tin oxide or zinc oxide. Although the illumination volume of the sample for the study reported here is about 1.4×10^{-3} μm^3, we have pushed the detection limit down to 1×10^{-4} μm^3 (Cai *et al.*, 2005). With improvements in zone-plate optics, we expect the detection limit will be pushed further to 10^{-5} to 10^{-6} μm^3 in the near future. We believe that future research into understanding the structure-related electrical, thermal and optical transport processes in nanoscale materials will benefit from the development of the X-ray nanodiffraction technique and its applications.

Use of the Advanced Photon Source was supported by the US Department of Energy, Office of Science, Basic Energy Science, under Contract No. W-31-109-ENG-38. The SEM analysis was performed in the Electron Microscopy Center, Materials Science Division, Argonne National Laboratory, Argonne, IL, USA.

electronic reprint

References

Arabatzis, I. & Falaras, P. (2003). *Nano Lett.* **3**, 249–251.

Cai, Z., Lai, B., Xiao, Y. & Xu, S. (2003). *J. Phys. IV*, **104**, 17–20.

Cai, Z., Lai, B., Yun. W., Ilinski, P., Legnini, D., Maser, J. & Rodrigues, W. (2000). *AIP Proc.* **507**, 472–477.

Cai, Z. *et al.* (2005). To be published.

Chen, Y., Cui, X., Zhang, K., Pan, D., Zhang, S., Wang, B. & Hou, J. (2003). *Chem. Phys. Lett.* **369**, 16–20.

Dejus, R. J., Vasserman, I. B., Sasaki, S. & Moog, E. R. (2002). Report ANL/APS/TB-45. Argonne National Laboratory, Argonne, IL, USA.

Dillon, C. T., Lay, P. A., Kennedy, B. J., Stampfl, A. P. J., Cai, Z., Ilinski, P., Rodrigues, W., Legnini, D. G., Lai, B. & Maser, J. (2002). *J. Biol. Inorg. Chem.* **7**, 640–645.

Eastman, D. E., Stagarescu, C. B., Xu, G., Mooney, P. M., Jordan-Sweet, J. L., Lai, B. & Cai, Z. (2002). *Phys. Rev. Lett.* **88**, 156101.

Evans, P. G., Issacs, E. D., Aeppli, G., Cai, Z. & Lai, B. (2002). *Science*, **295**, 1042–1045.

Goldberger, J., He, R., Zhang, Y., Lee, S., Yan, H., Choi, H. & Yang, P. (2003). *Nature (London)*, **422**, 599–601.

Hall, M. D., Dillon, C. T., Zhang, M., Beale, P., Cai, Z., Lai, B., Stampfl, A. P. J. & Hambley, T. W. (2003). *J. Biol. Inorg. Chem.* **8**, 726–732.

Howells, H. (1995). *Opt. Eng.* **34**, 410–417.

Kirkpatrick, P. & Baez, V. (1948). *J. Opt. Soc. Am.* **38**, 766–774.

Lai, B., Yun, W., Legini, D., Xiao, Y., Chrzas, J., Viccaro, P. J., White, V., Bajikar, S., Denton, D., Cerrina, F., Difabrizio, E., Gentili, M., Grella, L. & Baciocchi, M. (1992). *Appl. Phys. Lett.* **61**, 1877–1879.

Libera, J., Cai, Z., Lai, B. & Xu, S. (2002). *Rev. Sci. Instrum.* **73**, 1506–1508.

Liu, S., Yue, J. & Wehmschulte, R. (2002). *Nano Lett.* **2**, 1439–1442.

Liu, Y., Dong, Y. & Wang, G. (2002). *Appl. Phys. Lett.* **82**, 260–262.

Maniwa, Y., Kataura, H. & Fujiwara, A. (2003). *J. Jpn. Soc. Synchrotron Rad. Res.* **16**, 296–305.

Murken, G. von & Tromel, M. (1973). *Z. Anorg. Allg. Chem.* **397**, 117–126.

Pan, Z., Dai, Z. & Wang, Z. (2001). *Science*, **291**, 1947–1949.

Raola, O. & Strouse, G. (2002). *Nano Lett.* **2**, 1443–1447.

Snigirev, A., Kohn, V., Snigireva, I. & Lengeler, B. (1996). *Nature (London)*, **384**, 49–51.

Soh, Y. A., Evans, P. G., Cai, Z., Lai, B., Kim, C. Y., Aeppli, G., Mathur, N. D., Blamire M. G. & Isaacs, E. D. (2002). *J. Appl. Phys.* **91**, 7742–7744.

Wang, W., Xu, C., Wang, X., Liu, Y., Zhan, Y., Zheng, C., Song, F. & Wang, G. (2003). *J. Mater. Chem.* **12**, 1922–1925.

Wang, W., Xu, C., Wang, G., Liu, Y. & Zheng, C. (2002). *J. Appl. Phys.* **92**, 2740–2742.

Wen, X., Zhang, W., Yang, S., Dai, Z. & Wang, Z. (2002). *Nano Lett.* **2**, 1397–1401.

Xu, C., Zhao, X., Liu, S. & Wang, G. (2003). *Solid State Commun.* **125**, 301–304.

Yun, W., Pratt, S. T., Miller, R. M., Cai, Z., Hunter, D. B., Jarstfer, A. G., Kemner, K. M., Lai, B., Lee, H. R., Legnini, D. G., Rodrigues, W. & Smith, C. I. (1998). *J. Synchrotron Rad.* **5**, 1390–1395.

Yun, W., Vicarro, P. J., Lai, B. & Chrzas, J. (1992). *Rev. Sci. Instrum.* **63**, 582–585.

electronic reprint